11th World Congress on Computational Mechanics (WCCM XI)
5th European Conference on Computational Mechanics (ECCM V)
6th European Conference on Computational Fluid Dynamics (ECFD VI)
E. Oñate, J. Oliver and A. Huerta (Eds)

MODELLING UNDER-EXPANDED JET SCREECH BY ILES

ALESSANDRO MANCINI*, DANILO DI STEFANO†, EDWARD H. HALL‡ AND ALDO RONA§

Department of Engineering, University of Leicester, LE1 7RH, England
* e-mail: am791@leicester.ac.uk, † e-mail: dds13@leicester.ac.uk
‡ e-mail: eh171@leicester.ac.uk, § e-mail: ar45@leicester.ac.uk
web page: http://www.le.ac.uk/eg/ar45

Key words: Implicit Large Eddy Simulations, Jet, Screech, Numerical Methods.

Abstract. Axisymmetric screech from an under-expanded contoured sonic nozzle is modelled by Implicit Large Eddy Simulations (ILES). A self-sustained shear-layer instability develops naturally, without artificial excitation, in the time-marching ILES simulation. This reproduces some of the main flow characteristics of the A2 axisymmetric screech mode documented in experiment. This includes a tonal pressure field, which is resolved by the model. The axisymmetric modelling approach prevents the development of azimuthal structures in the jet shear-layer downstream of the potential core, which are known to be important features for controlling jet mixing and broad-band jet noise.

1 INTRODUCTION

High-speed fighter aircraft feature low-bypass engines where the dominant noise source is the aerodynamic jet noise, which can feature an intense tonal noise, commonly referred to as a screech tone. The origin of screech stems from operating the jet incorrectly expanded, whereupon a system of shock cells interacts with convected instabilities in the jet outer shear-layer, generating noise [1].

The selection of convectively amplifying shear-layer instabilities by upstream feed-back locks the noise generation process in a feed-back loop, which determines the tonal characteristic of screech. From a computational viewpoint, screech therefore involves mainly a narrow band of the kinetic energy spectrum in the jet shear layer. This makes the problem treatable by a numerical approach that resolves directly the relevant scales of motion associated to screech and models the effects of any under-resolved smaller-scale dynamics on the resolved motion. Such an approach has been followed in the form of an Implicit Large Eddy Simulation (ILES).

Jet screech can feature a combination of axisymmetric modes, commonly denoted as A modes, and of spiral modes, or B modes, depending on the degree of incorrect expansion [2]. The most acoustically active source region in an incorrectly expanded jet stretches

from the proximity of the nozzle lip, where the high-frequency contribution mainly originates from the interaction of small amplitude shear-layer disturbances with the intense shocks and expansion waves, to the end of the jet potential core, where the shear-layer instabilities, which have grown to finite amplitude, interact with the weaker shock-cell system. The shock-cell spacing close to the nozzle exit plane is mainly determined by the inviscid compressible momentum-energy balance and is progressively affected by the growth rate of the jet shear layer at increasing axial distances.

Incorrectly expanded jets from nozzles operating close to their design Mach numbers, such as Mach 1 for convergent nozzles, exhibit an axisymmentric instability mode [3], leading to an axisymmetric screech noise pattern, when screech is present. At these conditions, a time-resolved simulation of the shock cells enclosed in the thin shear-layer in the early stages of streamwise growth, close to the nozzle lip, is expected to be able to capture the main mechanisms responsible for the generation of screech. This approach is implemented by performing an axisymmetric Implicit Large Eddy Simulation of an incorrectly expanded jet. The absence of the azimuthal degree of freedom in the computation limits the growth of secondary, spiral mode instabilities in the shear-layer. As a consequence, the shear-layer is expected to exhibit a reduced growth rate downstream of the end of the potential core.

The aim of this research is to explore the use of axisymmetric Implicit Large Eddy Simulations as a lower computational cost technique, compared to three-dimensional Large Eddy Simulations, for modelling the compressible flow dynamics of a screeching jet close to the nozzle exit and for predicting the dominant narrow-band components of the radiating unsteady pressure near-field.

2 FLOW CONDITIONS

Axisymmetic Implicit Large Eddy Simulations are obtained for a contoured convergent nozzle designed for parallel flow at exit. The nozzle design exit Mach number M_e is 1.0. The simulation is designed to match the geometry and the experimental flow conditions tested by André [4]. At the nozzle exit plane, the inner nozzle diameter is 38 mm and the nozzle lip is 0.5 mm thick. The nozzle is supplied with unheated air at a nozzle pressure ratio of 2.27, corresponding to a fully expanded isentropic exit Mach number $M_j = 1.15$. Over a range of nozzle operating conditions, experiments found the turbulence intensity at the nozzle exit plane to be about 2% [4]. The jet discharges in ambient quiescent air at pressure $p_a = 98$ kPa and temperature $T_a = 288.15$ K. The Reynolds number based on the nozzle exit diameter and flow conditions is 1.2×10^6. The air flow is modelled under constant specific heat ideal gas assumptions, with the specific gas constant $R = 287.058$ J/(kg K) and the specific heat ratio $\gamma = 1.4$.

3 NUMERICAL METHOD

At the selected flow conditions, the jet under-expansion develops an axisymmetric A2 screech mode [4]. Tam and Hu [5] showed that this aero-acoustic phenomenon is mainly an inviscid process, involving the convective amplification of shear-layer instability modes, their interaction with the shock-cell structure, and an intense tonal acoustic feed-back through the subsonic portion of the shear-layer to the nozzle lip. The characteristic frequency of this self-excited process is typically tonal and well defined, prompting the adoption of a modelling approach in which this frequency and its associated large-scale motion are resolved in space and time.

In view of the stated focus on resolving the unsteady pressure near-field, the higher-frequency motion mainly associated to the small-scale turbulence is not resolved. A space filtering criterion can then be introduced by which the flow governing equations, the compressible Navier-Stokes equations, are top-hat filtered by the unit cell volume Δ of the computational mesh. In the filtered equations, each scalar variable f is represented by the summation of its top hat filtered value, $< f >$, plus a fluctuation f'', so that $f =< f > +f''$. Upon neglecting product terms involving the small-scale density and temperature fluctuations, the resulting equations are formally identical to the Reynolds averaged Navier-Stokes equations. In Large Eddy Simulations (LES), products of the fluctuating quantities are modelled based on the filtered quantities, to provide turbulence closure. In Implicit Large Eddy Simulations, the effects the fluctuating quantities have on the filtered quantities are taken as mainly diffusive and dissipative and the numerical dissipation and diffusion in the numerical scheme is relied upon to model such effects. By this approach, all products of fluctuating quantities $< f''f'' >$ in the filtered equations are set to zero, thereby reducing the computational effort compared to a Large Eddy Simulation.

The resulting governing equations in ILES are formally identical to the Navier-Stokes equations. In cylindrical coordinates (x, r, θ), the axisymmetric flow governing equations are

$$\frac{\partial \mathbf{U}}{\partial t} + \frac{\partial \mathbf{F}}{\partial x} + \frac{\partial r\mathbf{G}}{r\partial r} = \frac{\partial \mathbf{F}_v}{\partial x} + \frac{\partial r\mathbf{G}_v}{r\partial r}, \tag{1}$$

where the vector of the conservative variables $\mathbf{U}$ and the inviscid $(\mathbf{F}, \mathbf{G})$ and viscous $(\mathbf{F}_v, \mathbf{G}_v)$ flux vectors are

$$\begin{aligned}
\mathbf{U} &= (\rho, \rho u_x, \rho u_r, \rho e_s)^T, \\
\mathbf{F} &= \left(\rho u_x, \rho u_x^2 + p, \rho u_x u_r, \rho u_x h_s\right)^T, \\
\mathbf{G} &= \left(\rho u_r, \rho u_r u_x, \rho u_r^2 + p, \rho u_r h_s\right)^T, \\
\mathbf{F}_v &= (0, \tau_{xx}, \tau_{xr}, u_x\tau_{xx} + u_r\tau_{xr} + q_x)^T, \\
\mathbf{G}_v &= (0, \tau_{rx}, \tau_{rr}, u_x\tau_{rx} + u_r\tau_{rr} + q_r)^T,
\end{aligned} \tag{2}$$

where superscript T denotes vector transpose. Equation 2 is stated in terms of space-filtered variables normalised with respect to the nozzle exit plane conditions (ρ_e, u_e, T_e),

where the symbol <> is omitted for conciseness, as in the remainder of this paper. Lengths are normalised by the nozzle exit diameter D_e, density ρ by ρ_e, velocities (u_x, u_r) by u_e, pressure p by $\rho_e u_e^2$, specific stagnation enthalpy h_s and specific stagnation energy e_s by u_e^2, temperature T by T_e, time t by D_e/u_e, and molecular viscosity μ by μ_e. The ideal gas state equation $p = \rho T/\left(\gamma M_e^2\right)$ relates p, ρ, and T. The viscous stress tensor τ is

$$\begin{aligned}
\tau_{xx} &= 2\frac{\mu}{Re}\frac{\partial u_x}{\partial x} - \frac{2}{3}\frac{\mu}{Re}\left(\frac{\partial u_x}{\partial x} + \frac{\partial r u_r}{r\partial r}\right), \\
\tau_{rr} &= 2\frac{\mu}{Re}\frac{\partial u_r}{\partial r} - \frac{2}{3}\frac{\mu}{Re}\left(\frac{\partial u_x}{\partial x} + \frac{\partial r u_r}{r\partial r}\right), \\
\tau_{xr} &= \tau_{rx} = \frac{\mu}{Re}\left(\frac{\partial u_x}{\partial r} + \frac{\partial u_r}{\partial x}\right)
\end{aligned} \tag{3}$$

and the heat flux vector is

$$\begin{aligned}
q_x &= \frac{1}{(\gamma-1)\,M_e^2 Re}\frac{\mu}{Pr}\frac{\partial T}{\partial x}, \\
q_r &= \frac{1}{(\gamma-1)\,M_e^2 Re}\frac{\mu}{Pr}\frac{\partial T}{\partial r},
\end{aligned} \tag{4}$$

where Pr is the Prandtl number. The molecular viscosity μ is estimated by Sutherland's law

$$\mu = 1.458 \times 10^{-6}\left(\sqrt{T_e}/\mu_e\right) T^{3/2}/\left(T - 110.4/T_e\right). \tag{5}$$

The specific stagnation energy e_s and the specific stagnation enthalpy h_s are given by

$$e_s = T/\left[\gamma\left(\gamma-1\right)M_e^2\right] + \left(u_x^2 + u_r^2\right)/2, \tag{6}$$

$$h_s = e_s + p/\rho. \tag{7}$$

The finite-volume discrete form of the flow governing equations, Eq. 1, are applied to the jet computational domain of Fig. 1, where only the top half of the meridional plane through the jet axis is shown for clarity. The computational domain extends $6D_e$ radially and $20.5D_e$ axially and is discretised by a structured computational mesh. Two meshes, shown in Fig. 2, have been produced by a bespoke in-house mesh generator, coded in Fortran 77. The first is a uniform rectangular mesh comprising 1313×385 nodes with a constant square cell size $(\Delta x, \Delta r)$ $15.625 \times 10^{-3} D_e$ by $15.625 \times 10^{-3} D_e$ on the (x, r) plane. This mesh is shown if Fig. 2(b) where one every 6 grid lines is plotted, for clarity. Adopting a uniform spatial discretisation in this plane has the advantage that, for axisymmetric flows, the same spatial filter Δ is applied consistently to the governing equations, resulting in a uniform filtering effect with a constant cut-off wavenumber in Fourier space. The second computational mesh has the same 1313×385 size as the uniform mesh and uses the same uniform axial spacing Δx. The radial spacing is non-uniform, with cells clustered either side of the nozzle lip. The radial mesh clustering is determined by a parabolic radial

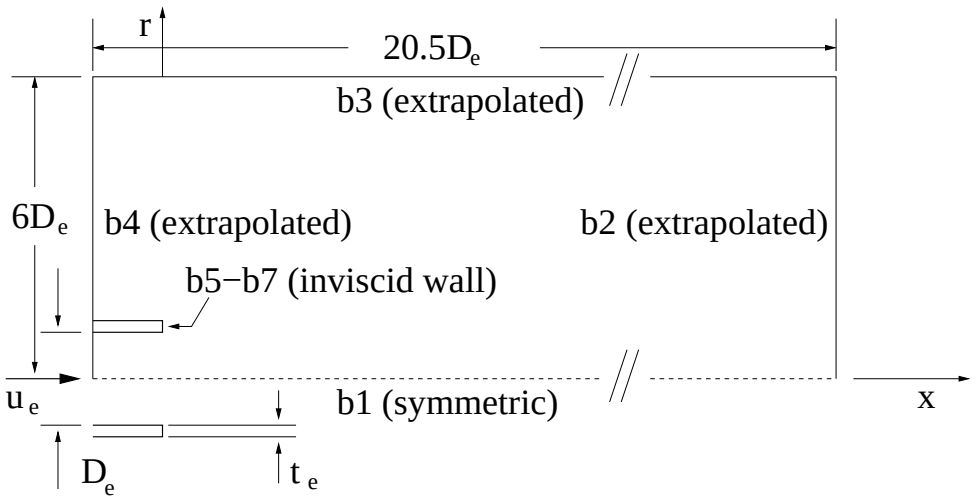

Figure 1: Computational domain and boundary conditions.

size distribution function with the minimum $\Delta r = 2.63 \times 10^{-3} D_e$ located at the nozzle lip radius. The resulting mesh is shown in Fig. 2(a), where one every 6 grid lines in x and r is plotted, for clarity. This mesh non-uniformity in r enables a greater local spatial resolution close to the nozzle lip, where the shear-layer is radially thin, and reduces the computational resources required away from the jet axis, where long-wavelength acoustic waves are expected to radiate in the ambient flow.

On the radially stretched mesh, the nozzle internal diameter D_e and the nozzle lip thickness t_e have the same size as in experiment [4] at the nozzle exit plane. On the uniform mesh, the nozzle internal diameter D_e at the nozzle exit plane matches the experiment but the nozzle lip is thicker than in experiment.

The jet flow is characterised by compressible features, such as shocks, expansion fans, and regions of significant flow shear. These features produce significant localised gradients in the conservative variables. To resolve these features, a time-marching Total Variation Diminishing (TVD) scheme is used to integrate the space-filtered flow governing equations in finite-volume form. The inviscid fluxes at the computational cell interfaces are evaluated using the second-order form of the Roe [6, 7] flux difference approximate Riemann solver in the interface-normal direction. Numerical stability is provided by applying the min-mod flux limiter. Second-order central differences are used to evaluate the viscous fluxes at the cell interfaces.

The computation is time-marched by a two-step Runge-Kutta scheme implemented in the low storage form of Hu et al. [8]. The standard Runge-Kutta coefficients $(1.0, 0.5)$ are used. A further description of this numerical integration procedure can be found in Rona and Zhang [9].

Along the perimeter of the computational domain, boundary conditions are imposed as

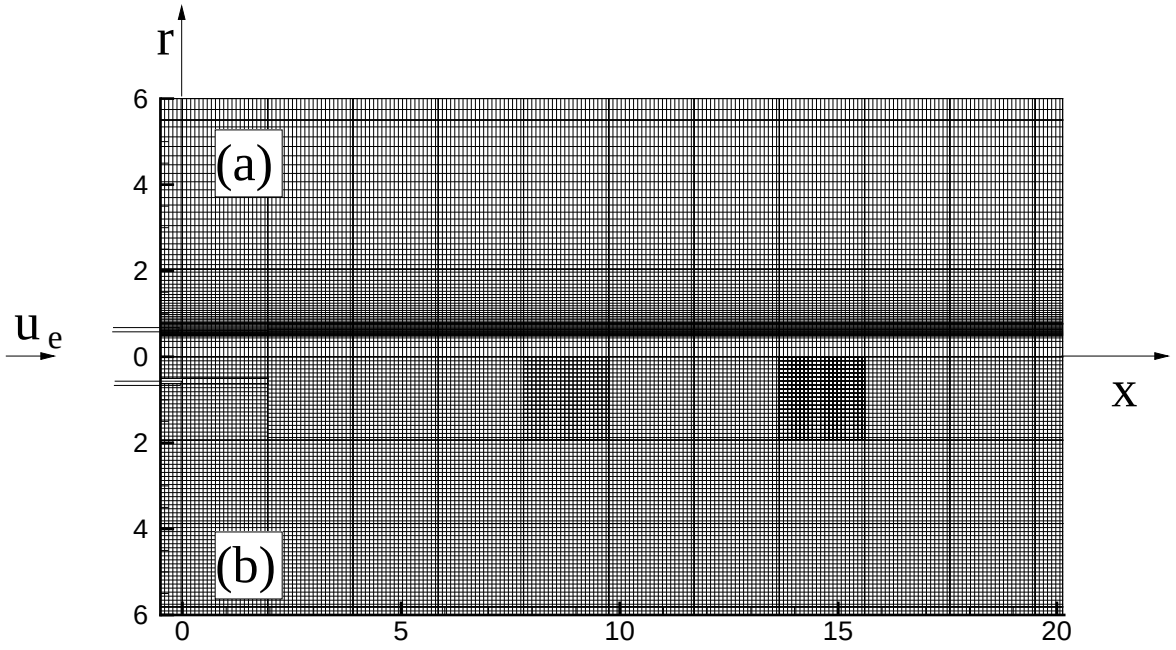

Figure 2: (a) Radially stretched computational mesh, (b) Uniform computational mesh.

shown in Fig. 1. A reflecting boundary b1 is imposed along the jet axis where $\mathbf{U}_{i,-j} = \mathbf{U}^*_{i,j}$ for $j = 1$ and $j = 2$, where $r = j\Delta r$ and $\mathbf{U}^* = (\rho, \rho u_x - \rho u_x \Delta i, \rho u_r - \rho u_r \Delta j, \rho e_s)^T$. The open flow boundaries b2-b4 are treated by a linear extrapolation of flow state from the computational domain interior. The solid boundaries b5-b7 are modelled by the wall condition $r\mathbf{U}_{i,-j} = r\mathbf{U}^*_{i,j}$ for $j = 1$ and $j = 2$ and $\mathbf{U}_{-i,j} = \mathbf{U}^*_{i,j}$ for $i = 1$ and $i = 2$ for the horizontal and vertical surfaces, respectively. At the nozzle inlet, a constant flow state (ρ_e, u_e, T_e, M_e) is imposed throughout the computation.

At the start of the computation, the computational domain outside the nozzle is primed with the ambient zero flow conditions and the jet is impulsively started by the nozzle inlet supersonic inflow. This abrupt start condition challenges the computational stability of the scheme, as it generates a downstream propagating bow shock outside the nozzle. The flow was therefore uniformly time-marched by a variable time step corresponding to a maximum Courant number of 0.8. The variable time step is evaluated at every iteration as the maximum non-dimensional Δt that gives the target Courant number, based on the local computational cell geometry and the local flow conditions. The computations on the uniform and stretched meshes were time-marched to the non-dimensional times $t = 15.5/D_e$ and $t = 3.39/D_e$, respectively, to obtain a stationary flow, as indicated by the static pressure monitored at $x = 1.5D_e$ on the jet axis and along the nozzle lip line. By $t = 1/D_e$, the bow shock has propagated through the downstream boundary b2 of Fig. 1 and a jet with an organised shock-cell pattern is developed.

During this initial transient, an axisymmetric self-sustained shear-layer instability developed in the axisymmetric flow without forcing. The jet self-selected its shear-layer mode frequency f and Strouhal number $Str = fD_e/u_e$. Fourier analysis of the monitored static pressure on the uniform mesh simulation indicated two spectral peaks, with the lowest (fundamental) screech Strouhal number $Str = 0.6958$. The combination of the removal of the strong bow shock by its propagation through the computational boundaries and the stabilising effect of the viscous dissipation allowed the computation to time-advance at larger variable time-steps, compared to when the bow shock was present, still keeping the constant Courant number of 0.8.

After the flow has settled into a self-sustained shear-layer fluctuation flow regime, characterised by a substantially time-invariant fundamental screech frequency, the time-averaged flow field was obtained from the time-dependent computation as a running average of the primitive variables (ρ, u_x, u_r, p). On the uniform mesh, the running average was obtained between the non-dimensional times of $t = 15.5/D_e$ and $t = 17.15/D_e$, corresponding to 30 periods $T = 1/f$ of the measured screech mode frequency $f = 5841$ Hz [4]. Root-mean-square averages of the primitive variables were obtained alongside the mean values. On the radially stretched mesh, a longer running average between non-dimensional times of $t = 3.39/D_e$ and $t = 6.25/D_e$ was used.

4 RESULTS

4.1 Time-averaged flow predictions compared to experiment

Figure 3 shows the Mach number distribution, referenced to the local speed of sound c, along the jet axis. The numerical prediction from the uniform mesh, shown by the continuous line, is compared with measurements by André [4], denoted by $(\circ)$. The location and amplitude of the Prandtl-Mayer expansion fan at nozzle lip and the subsequent conical shock appear to be predicted well by just using an axisymmetric ILES computation. This is shown by the good match in axial location and value, between experiment and prediction, of the low Mach number at the nozzle exit, the sharp first static Mach number peak, and the subsequent Mach number minimum. Further downstream, while the spacing between subsequent Mach number maxima and minima is in broad agreement, the amplitude of the streamwise Mach number fluctuations is lower in the predictions compared to the experiment. This is likely to result from the axial precession of the shock cells, due to the shear-layer motion. The movement of the shock-cells during the running average causes shock smearing in the time-averaged flow, reducing the amplitude of the extrema in the axial Mach number distribution. As the shear-layer motion grows in amplitude with increasing downstream distance from the nozzle exit plane, the shock cells further away from the nozzle exit are more affected by this shock smearing process in the time-averaged flow, as indicated in Fig. 3. The same trend is displayed by the time-averaged Mach number distribution predicted by the radially stretched ILES.

Table 1 shows the comparison between the shock cell lengths predicted by the ILES

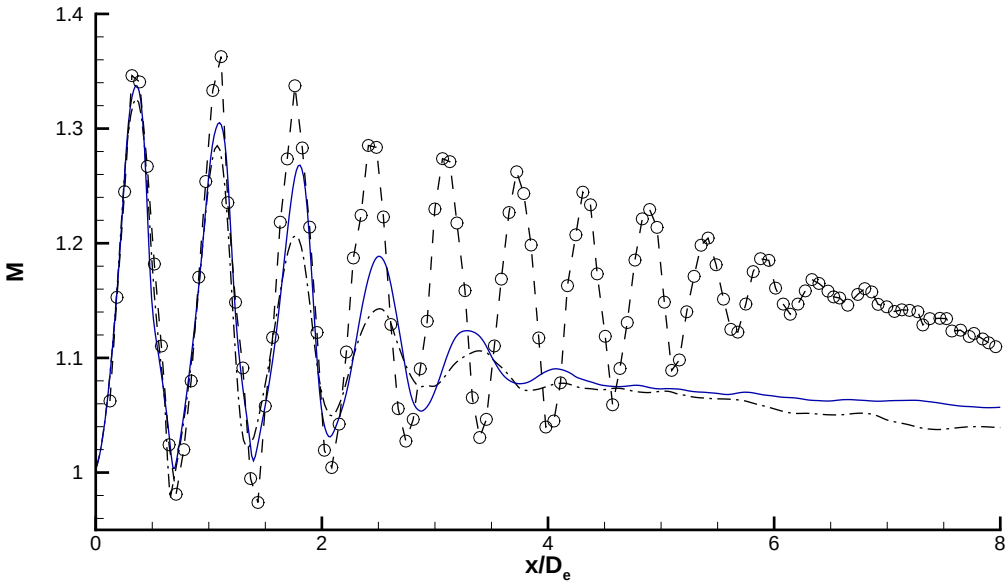

Figure 3: Mach number distribution along the jet axis. (−) ILES uniform mesh flow prediction averaged over $30T$, $(- \cdot -)$ ILES radially stretched mesh prediction averaged over $50T$, $(\circ)$ experiment [4].

using the uniform mesh and the ones reported in the measurements [4]. Both measurements and predictions indicate a monotonic reduction in shock cell length with axial distance. The shear layer grows in the downstream direction by entrainment of the low speed flow that surrounds it. Axial momentum transfer to the entrained fluid from the high-speed flow closer to the jet axis reduces the enclosed high-speed flow radius. The boundary between the shear layer and the high-speed flow is therefore convex and the axial velocity progressively reduces, due to the irreversible axial momentum loss through the shocks. This results in progressively more normal compression and expansion waves, which reduce the shock cell spacing in the axial direction. The predicted shock spacing is in broad agreement with experiment over the first three shock cells. Figure 3 indicates that the agreement in shock-cell length progressively decreases with increasing shock cell number. The shear layer thickness is smaller over the first three shock cells, increasing monotonically in the positive axial direction. As the time-averaged shear layer thickness is determined by the diffusive and dissipative effects in the flow momentum and, in the Implicit Large Eddy Simulation, these effects are numerical scheme dependent, further improvements in the numerical mesh and in the limiter function are likely to improve the current flow predictions.

Figure 4 shows the non-dimensional time-averaged density contours from the radially stretched ILES, Fig. 4(a), and from the uniform mesh ILES, Fig. 4(b). The pattern of alternating shock-cells close to the nozzle lip is shown in both simulations. The intensity

Table 1: Axial length of shock cells.

Shock spacing	ILES uniform mesh	ILES stretched mesh	Measurement [4]
L_1/D_e	0.72	0.72	0.73
L_2/D_e	0.73	0.69	0.68
L_3/D_e	0.69	0.73	0.68
$\bar{L}_{avg}/D_e$	0.71	0.71	0.70

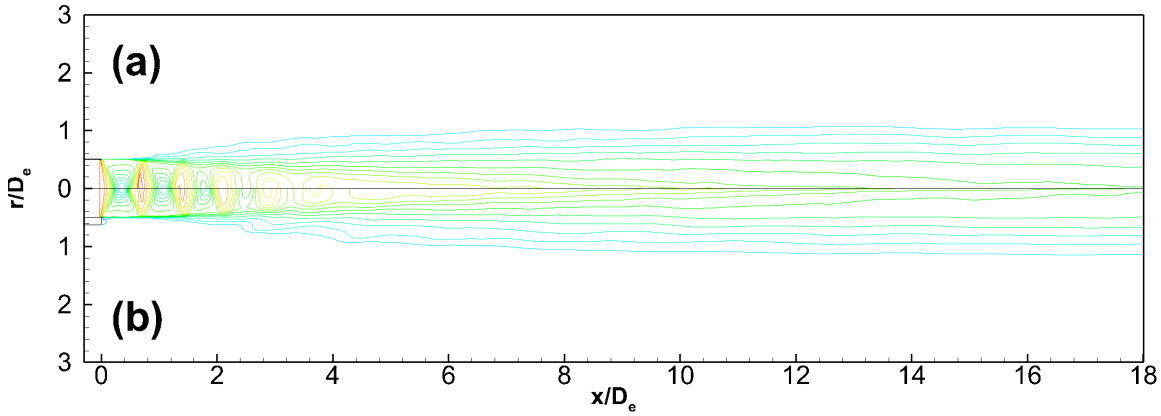

Figure 4: Non-dimensional time-averaged density contours. (a) radially stretched mesh ILES, (b) uniform mesh ILES. $\rho_{min} = 0.66\rho_e$, $\rho_{max} = 1.03\rho_e$, $\Delta\rho = 0.03\rho_e$.

of the shocks and expansions are shown to decrease with increasing axial distance from the nozzle exit plane. The waviness of the contours furthest from the jet axis suggest that the running average time may have been insufficient for producing a time-independent statistically converged mean flow. This feature is more evident in Fig. 4(b), where the mean field is estimated over the shorter non-dimensional averaging time $\Delta t = 1.65/D_e$.

4.2 Time-resolved flow predictions

Time-resolved flow predictions are obtained from both the uniform mesh simulation and from the radially stretched mesh simulation. The non-dimensional aerodynamic pressure monitored on the jet axis in Fig. 5(a) is unsteady, displaying fluctuations that have a rich yet narrow-band spectral content, as suggested by the presence of about 30 smooth pressure peaks over the non-dimensional sampling time of $1.65/D_e$. The Discrete Fourier Transform of the digital pressure history, shown in Fig. 5(b), confirms that the near-field aerodynamic pressure is characterised by one well-defined spectral peak. This compares to two spectral peaks identified in experiment [4] at 5171 Hz and 5841 Hz, corresponding to $Str = 0.617$ and 0.697. The dominant Strouhal number tone from the current simulation is 0.6958. A spectrogram analysis reported by André suggests that the modes associated to

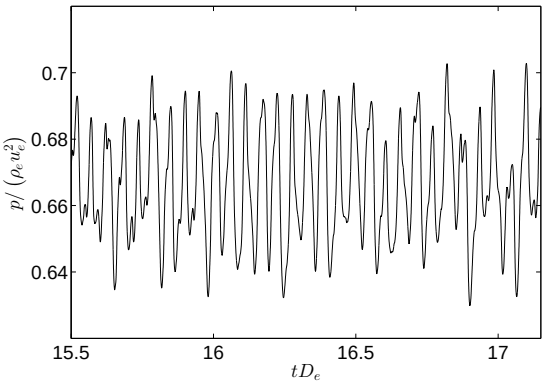

(a) Non-dimensional pressure history.

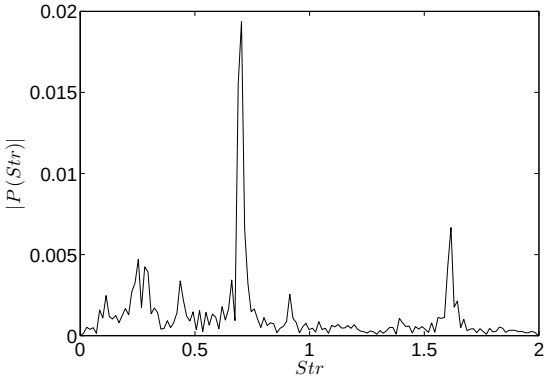

(b) Non-dimensional pressure spectrum.

Figure 5: Pressure at $(x, r) = (1.5D_e, 0)$ from the uniform mesh ILES.

these screech frequencies alternate over time and a similar mechanism has been observed by a similar spectrogram analysis of the numerical predictions from the uniform mesh ILES.

Time-resolved density snapshots of the under-expanded jet are reported in Fig. 6, covering three successive phases of the period T associated to the fundamental screech tone identified in the pressure spectrum of each ILES simulation. In both the uniform mesh and radially stretched mesh results, an intense shear-layer flow dynamics is predicted. This is characterised by the roll-up of toroidal vortices downstream of the nozzle lip line that grow in the streamwise direction as they are pushed by the core jet towards the downstream computational domain boundary. The passage of the vortices through the shock cells affect the position of the pressure waves that precess over time about their time-averaged position, confirming the inference of the 'shock smearing' effect in the time-averaged axial Mach number distribution from Fig. 3.

5 CONCLUSIONS

Axisymmetric Implicit Large Eddy Simulations are used as a reduced cost computational model for predicting the narrow-band tonal flow dynamics of an under-expanded jet in screech. The model restricts the resolved instability modes in the jet to axisymmetric (varicose) shear-layer instabilities that interact with the shock-cell pattern, producing large-amplitude near-field pressure fluctuations. The mainly inviscid nature of screech, which mainly involves the shock cells in the neighbourhood of the nozzle outlet, enables the use of such a reduced model that does not resolve the complex three-dimensional flow mixing characterizing the jet plume further downstream. Predictions of unsteady pressure and of time-averaged Mach number in broad qualitative agreement with the available experimental data indicate that, within limits, the axisymmetric simulation is a useful model for exploring the motion of the shear-layer and its interaction with the shock-cell structure.

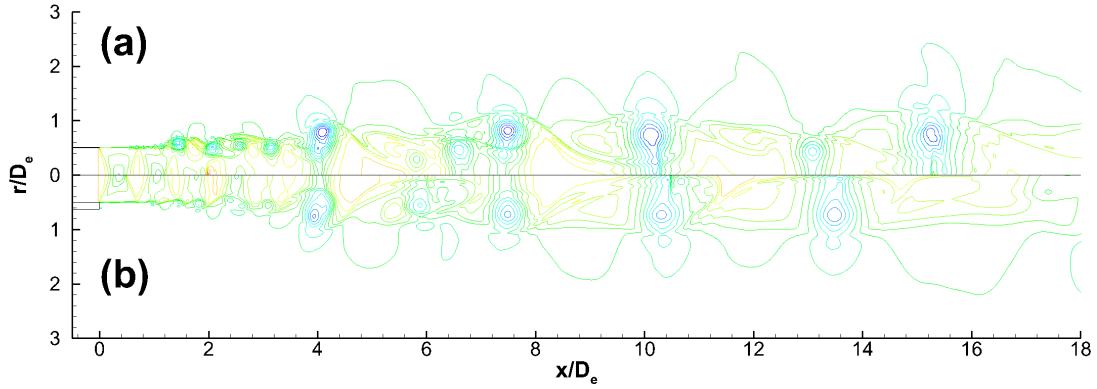

(a) Incremental non-dimensional time $\tau = 0.0$.

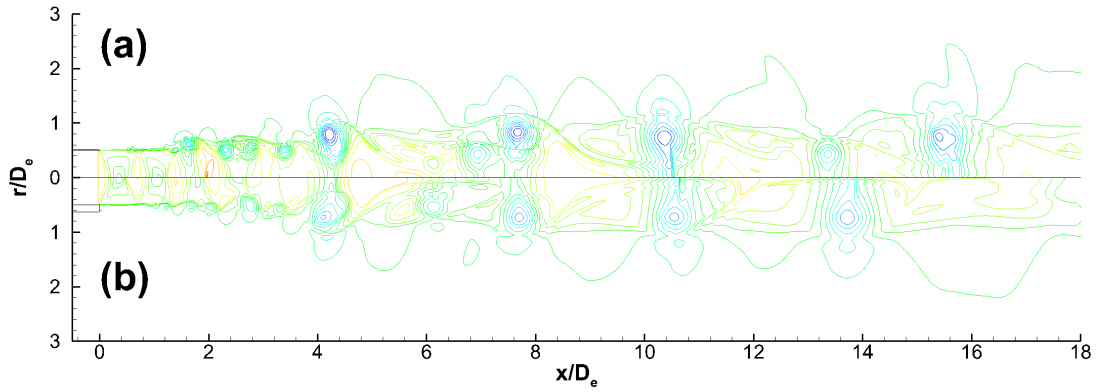

(b) Incremental non-dimensional time $\tau = T/4$.

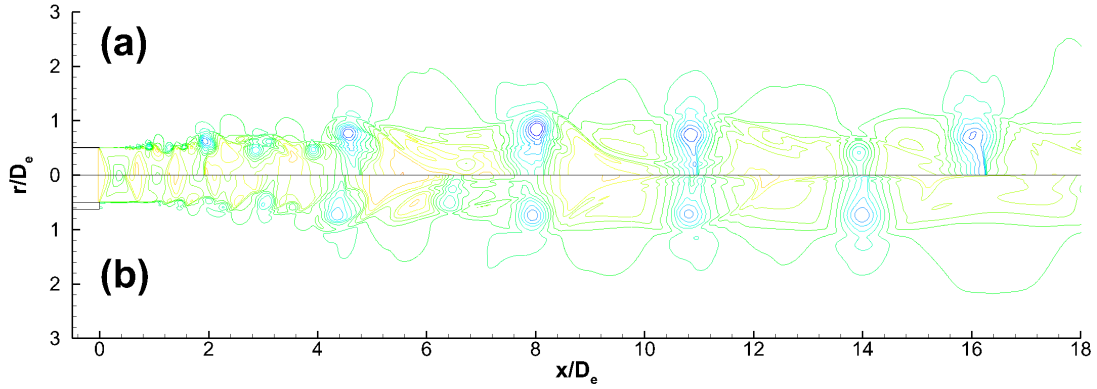

(c) Incremental non-dimensional time $\tau = T/2$.

Figure 6: Time-resolved non-dimensional density contours of the jet at incremental non-dimensional time (a) $\tau = 0.0$, (b) $\tau = T/4$, and (c) $\tau = T/2$. (a) radially stretched mesh, (b) uniform mesh. $\Delta\rho = 0.05\rho_e$.

6 ACKNOWLEDGEMENT

This work has received support from the European Union Seventh Framework Programme FP7/2007-2013 under grant agreement no. 317142. This paper has used digitized experimental data kindly provided by Carlos Pérez-Arroyo and Guillaume Puigt, CERFACS, France.

REFERENCES

[1] Harper-Bourne, M. and Fisher, M. The noise from shock waves in supersonic jets. AGARD Conference Proceedings 131, September 1973.

[2] Hubbard, H.H. *Aeroacoustics of flight vehicles : theory and practice*. NASA Reference Publication 1258, Woodbury, NY, (1995).

[3] Raman, G. Advances in understanding supersonic jet noise screech: Review and perspective. *Prog. Aerospace Sci.* (1998) **34**:45–106.

[4] André, B. *Étude expérimentale de l'effet du vol sur le bruit de choc de jets supersoniques sous-détendus*. PhD, École Centrale de Lyon, France, (2012).

[5] Tam, C. and Hu, F. On the three families of instability waves of high-speed jets. *Journal of Fluid Mechanics* (1989) **201**:447–483.

[6] Roe, P. Approximate Riemann solvers, parameter vectors and difference schemes. *Journal of Computational Physics* (1981) **43**:357–372.

[7] Roe, P. Characteristics-based schemes for the Euler equations. *Annual Review of Fluid Mechanics* (1986) **18**:337–365.

[8] Hu, F., Hussaini, M., and Manthey, J. Application of low dissipation and dispersion Runge-Kutta schemes to benchmark problems in computational aeroacoustics. *ICASE/LaRC workshop on benchmark problems in computational aeroacoustics (CAA)*, NASA Conference Publication 3300, (1995) 73–98.

[9] Rona, A. and Zhang, X. Time accurate numerical study of turbulent supersonic jets. *Journal of Sound and Vibration* (2004) **270**:297–321.